

# Effect of surface topology on the galloping instability of rectangular cylinders

Mark A. Feero<sup>a,\*</sup>, Ahmed M. Naguib<sup>b</sup>, Manoochehr M. Koochesfahani<sup>b</sup>

<sup>a</sup> Rowan, Williams, Davies and Irwin, Inc. Guelph, ON, Canada, N1G 4P6

<sup>b</sup> Department of Mechanical Engineering, Michigan State University, East Lansing, MI, 48823, USA

## ABSTRACT

The effect of geometry on the transverse galloping instability of rectangular cylinders was studied experimentally for Reynolds numbers between 1,000 and 10,000. In particular, a comparison was made between a rectangular cylinder with rounded corners and a smooth surface, and the same baseline geometry with added surface topology synthesized from two-dimensional Fourier-modes. The effects of the topology amplitude and wavelength were investigated. From measurements of the normal (galloping direction) force coefficient variation with angle-of-attack, it was found that the added surface topology generally had a destabilizing effect relative to the smooth cylinder. At the lowest Reynolds number, the smooth cylinder was stable, while the cylinders with added topology were unstable with respect to galloping. For Reynolds numbers from 5,000 to 10,000, the added topology did not cause a similar instability. However, there was a monotonic increase in the slope of the normal force coefficient at zero angle-of-attack with increasing surface height amplitude, thus moving the geometry closer to the instability threshold. This effect diminished as Reynolds number increased. Overall, for the range of parameters investigated herein, whenever the cylinders with topology were unstable to soft or hard galloping, the larger topology exhibited more favorable galloping resistance characteristics than the one with smaller topology. Topology wavelength was found to have no effect on the galloping behavior of the cylinder for Reynolds numbers below 7500, and a moderate increase in the normal force slope at zero angle of attack with decreasing wavelength for larger Reynolds numbers. The latter effect was associated with an increase in the angle of attack at which the cylinder could become unstable to hard galloping.

## 1. Introduction

This study is undertaken in light of recent findings that the suspension lines of Precision Air Drop Systems (PADS) may exhibit significant lateral vibration due to an aeroelastic instability known as galloping (Siefers et al., 2013, 2014). The resulting unsteady forces could adversely affect the overall performance and controllability of PADS (Bergeron et al., 2009). Thus, understanding the galloping behavior of parachute suspension lines is fundamental to the prediction and mitigation of this aeroelastic instability.

It is well known that elastically mounted cylinders with non-circular cross section may be susceptible to galloping. This is a result of the aerodynamic forces acting on the body varying with its orientation to the oncoming flow; as described schematically in Fig. 1 for a rectangular cylinder elastically mounted in the transverse ( $y$ ) direction. The lift and the drag forces,  $F_L$  and  $F_D$ , respectively, will be oscillatory in time due to the oscillation of the body at a velocity  $\dot{y}$ . The normal force coefficient in the  $y$ -direction is related to the lift and the drag coefficients, viz:

$$C_y = \frac{F_y}{0.5\rho U_\infty^2 dl} = -\frac{1}{\cos^2 \alpha} (C_L \cos \alpha + C_D \sin \alpha), \quad (1)$$

where  $C_L = F_L/(0.5\rho U_{rel}^2 dl)$  and  $C_D = F_D/(0.5\rho U_{rel}^2 dl)$  are the lift and the drag coefficients, respectively,  $\alpha$  is the instantaneous angle-of-attack,  $U_\infty$  is the steady freestream velocity,  $U_{rel}$  is the instantaneous

oncoming velocity relative to the cylinder,  $\rho$  is the density,  $d$  is the cylinder width and  $l$  is the cylinder span. If the oscillation is such that  $C_y$  increases with  $\alpha$ , this produces negative fluid damping and the structure may become unstable. Mathematically, the necessary aerodynamic condition for transverse galloping is  $\partial C_y / \partial \alpha > 0$ . This phenomenon can affect structures such as ice coated power lines, bridge decks and stalled wings (Blevins, 2001).

For a cylinder geometry that is unstable to galloping, the reduced flow velocity ( $U_R = U_\infty / f_y d$ , where  $f_y$  is the body's natural frequency of oscillation) has to exceed a critical reduced velocity  $U_{R,crit}$  for galloping to occur (Naudascher and Rockwell, 2009):

$$U_{R,crit} = \frac{4\pi Sc}{\left(\frac{\partial C_y}{\partial \alpha}\right)_{\alpha=0}}, \quad (2)$$

where  $Sc$  is the Scruton number, or the mass ratio-damping product. In air flows, the fluid density is typically much less than that of the oscillating structure, leading to a mass ratio of order  $10^3$ – $10^4$ , which with a typical damping ratio of order  $10^{-2}$  (Parkinson, 1989), leads to a Scruton number of the order  $10 - 10^2$ , and  $U_{R,crit}$  is of order  $10^2$ – $10^3$ . At such a high reduced velocity, the corresponding reduced frequency of galloping (or  $1/U_R$ ) is very low. Therefore, in air flows, galloping is predominantly analyzed under the assumption of quasi-steady flow conditions (Blevins, 2001; Naudascher and Rockwell, 2009; Parkinson, 1989).

\* Corresponding author.

E-mail address: [mark.feero@rwdi.com](mailto:mark.feero@rwdi.com) (M.A. Feero).

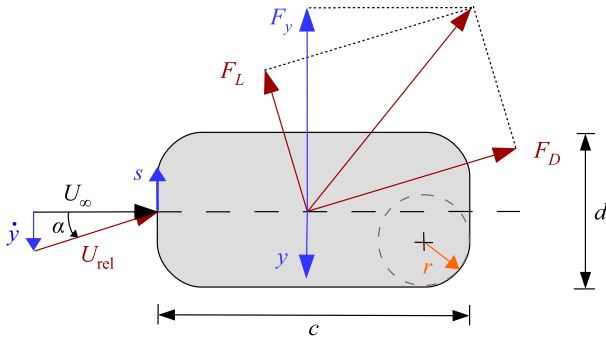


Fig. 1. Rectangular cylinder cross-section geometry and forces acting on the body when oscillating at a velocity  $\dot{y}$  in the transverse direction.

On the other hand, even in air, galloping could occur with relatively low mass ratio (e.g., order  $10^2$  for chimneys Parkinson and Wawzonek, 1981 and other light structures) and/or low damping (e.g., order  $10^{-3}$  in structures such as bridges Stoyanoff, 2001), leading to  $U_{R,crit}$  as low as order 10. In addition, in water flows the mass ratio is typically of order 1–10 (Parkinson, 1989), and hence  $U_{R,crit}$  is of order 0.1–10. In these situations,  $U_{R,crit}$  overlaps with the reduced-velocity range of vortex-induced vibration ( $U_s = U_\infty/f_s d = 1/St_s \approx 5 - 10$ , where  $f_s$  is the frequency of vortex shedding, and  $St_s$  is the corresponding Strouhal number). Under such conditions, vortex-induced and galloping oscillations interact and the assumption of quasi-steadiness breaks down (Parkinson, 1989).

A typical PADS suspension line has a non-circular cross section that resembles a rectangle with side ratio  $c/d = 2 - 3$  (where  $c$  is chord length) and rounded corners (Siefers et al., 2013). Much of the present understanding of the galloping behavior of rectangular cylinders is based on cross-sections with sharp corners. It is well established that these cylinders are prone to galloping in the side-ratio range  $c/d \approx 0.75 - 3$  in the absence of freestream turbulence. Parkinson (1989) connects the dependence on the side ratio to the significance of the afterbody, which is defined as the length of the cylinder's surface downstream of the separation points. For the sharp-corner rectangle, separation occurs at the upstream corners, and for  $c/d < 0.75$ , the afterbody is too short for the vortices forming in the separated shear layer to interact with the cylinder side surface (Nakamura and Tomonari, 1977). Such an interaction is necessary for establishing a secondary flow that produces a surface pressure distribution favorable to galloping (Parkinson, 1989). On the other hand, if the afterbody is sufficiently long ( $c/d$  larger than approximately 3), the shear layers reattach on the sides of the cylinder, and vortices are produced from separation of the shear layers at the trailing-edge corners, with no afterbody to interact with. This leads to stability to galloping for  $c/d \approx 3$ , and larger side ratios (Parkinson, 1989).

Recently, Feero et al. (2020) conducted a study focused on the Reynolds number range relevant to galloping of PADS ( $1000 \leq Re_d = U_\infty d/\nu \leq 10,000$ , where  $\nu$  is the kinematic viscosity). They found that a sharp-corner rectangular section, with a sufficiently-long afterbody to be stable to galloping ( $c/d = 3$ ), becomes unstable as the Reynolds number is decreased below a certain value. This finding was rather surprising given the insensitivity of the boundary layer separation location to Reynolds number. Feero et al. (2020) used surface pressure data to hypothesize that the reattachment of the shear layers on the sides of cylinders with long afterbody is a necessary but not sufficient condition for stability to galloping. Specifically, they noted that the reattachment point on the bottom surface of the cylinder (for positive angle of attack) must also shift upstream with increasing  $\alpha$  for the rectangular section to be stable to galloping. Their results showed that in the range  $\alpha = 0^\circ - 5^\circ$ , this shift occurs for Reynolds number based on the cylinder thickness of  $Re_d \geq 5000$  but not at lower Reynolds numbers

(as seen from their pressure measurements at  $Re_d = 1100$ ). Additional unusual behavior observed in the range  $Re_d < 5000$  included the sharp-corner rectangular section becoming more unstable to galloping with increasing  $c/d$  in the range 1–3 (manifested in the increase of the positive magnitude of  $\partial C_y/\partial \alpha|_{\alpha=0}$ , which would lead to smaller  $U_{R,crit}$ ), and the non-monotonic effect of various parameters on galloping instability for rectangular sections with rounded corners. The authors also commented that, given the predominant focus of galloping literature on the range  $Re_d > 10,000$ , the unique behavior below  $Re_d = 5000$  had not been brought into focus previously.

Flow-induced vibration of PADS suspension lines is a complex problem with several attributes including: unique geometry that may change dynamically due to stretching and twisting of the lines; different possible oscillation modes (transverse, torsional and coupled oscillation); yaw and pitch orientation with respect to the approach stream; and multi-line interactions. The present study is part of a foundational investigation into the fundamental aerodynamics underlying the vibration of suspension lines. As such, to attain good understanding of the physics associated with the various complexities, we take the approach of starting with the simplest aspects of the problem, and then gradually add these complexities into the investigation. The current study is focused on understanding how unique aspects of the suspension-line geometry might affect the possibility of transverse galloping of the lines within the Reynolds number range relevant to the operation of PADS ( $Re_d = 1000 - 10,000$ ). While (Siefers et al., 2013, 2014) concluded that the vibration of the lines is most likely caused by galloping, it was not known if the cross-section shape of the line is nominally unstable to galloping. It is also unknown how this instability might change with  $Re_d$  over the range 1000–10,000, where interesting flow physics relevant to galloping remain unexplored, as discussed above.

The goal of the present work is to experimentally investigate the galloping instability characteristics of rectangular cylinders that approximate the geometry of parachute suspension lines. A parachute line is often formed by braiding smaller lines, therefore the surface is not smooth but has variations in height that are generally of order  $\mathcal{O}(0.01d) - \mathcal{O}(0.1d)$ . An investigation regarding this type of geometry has not previously been performed, except by Siefers et al. (2013) and Siefers et al. (2014) who observed flow-induced vibrations of parachute suspension lines in a wind tunnel, analyzed the vortex shedding frequencies from the lines, and carried out flow visualization around a scaled-up solid model of the suspension line in a water tunnel. The present study investigates the aerodynamic forces and galloping instability of rectangular cylinders with smooth surfaces and those with an idealized surface topology with parameters approximating that of a parachute line. In particular, the effects of topology amplitude and wavelength are the focus of this study. Given the operation of PADS in air, it is highly likely that any galloping of the suspension line would occur at a frequency that is much smaller than that of vortex shedding from the line. Hence, the assumption of quasi-steadiness would be appropriate in analyzing galloping, and the results from static wind-tunnel tests can be used to describe the variation of aerodynamic forces with angle-of-attack. Consequently, in this work, measurements of aerodynamic loads are performed on rigidly mounted, static models with varying angle-of-attack.

## 2. Experimental setup

Experiments are conducted in a low-speed, low-turbulence open return wind tunnel located in the Flow Physics and Control Lab at Michigan State University. After passing through a section of flow management devices and a 10:1 contraction, the flow enters a 355 mm by 355 mm square test section that is 3 m long. The experiments in this work span a Reynolds number range of  $Re_d = 1100$  to 10,000, which corresponds to  $U_\infty \approx 0.8$  m/s to 7.5 m/s. The freestream velocity is monitored using a pitot-static tube connected to an MKS Baratron 223B differential pressure transducer with a full-scale range of 133 Pa and a

**Table 1**Experimental model geometries. All models have  $c/d = 2.5$  and  $r/d = 0.5$ .

| Description | $\epsilon_o/d$ (%) | $n$ | $\lambda_s/d$ | $\lambda_z/\lambda_s$ |
|-------------|--------------------|-----|---------------|-----------------------|
| Smooth      | 0                  | –   | –             | –                     |
| Topology    | 5                  | 10  | 0.61          | 1.5                   |
| Topology    | 10                 | 10  | 0.61          | 1.5                   |
| Topology    | 5                  | 20  | 0.31          | 1.5                   |

0.3% of-reading accuracy. At the low Reynolds number end, the pressure transducer resolution becomes a greater source of uncertainty than the accuracy, with a resolution of 0.013 Pa. The relative uncertainty in the measurement of  $Re_d$  varies from 2% to 0.5% for  $Re_d = 1100$  to 10,000. Over the range of freestream velocities used in this study, the mean turbulence intensity in the test section is 0.1% for a frequency range from 0.5 Hz to 10 kHz. The mean velocity uniformity in the test section is within 0.5% of the cross-section-averaged value.

The geometric parameters of the models under investigation are selected to approximate a typical flat parachute suspension line, both with and without the surface topology representative of braided cables. Based on the work of Siefers et al. (2013), the basic cross-sectional dimensions of the models used in this study are  $c/d = 2.5$  and  $r/d = 0.5$ . The surface topology of the braided cables is approximated using two-dimensional Fourier-modes to describe the height of the surface relative to the local nominal smooth cylinder. The local surface height,  $\epsilon$ , is defined as:

$$\frac{\epsilon}{\epsilon_o} = \frac{1}{2} \cos \left[ 2\pi \left( \frac{s}{\lambda_s} + \frac{z}{\lambda_z} \right) \right] + \frac{1}{2} \cos \left[ 2\pi \left( \frac{s}{\lambda_s} - \frac{z}{\lambda_z} \right) \right], \quad (3)$$

where  $s$  and  $z$  are the wall-tangential and axial coordinates, respectively,  $\epsilon_o$  is the surface height amplitude, and  $\lambda_s$  and  $\lambda_z$  are the wavelengths in the  $s$  and  $z$  directions, respectively. The  $s$ -direction wavelength can also be defined as  $\lambda_s = P/n$ , where  $n$  is the number of wavelengths in the  $s$ -direction and  $P$  is the perimeter. In order to avoid discontinuities in the surface,  $n$  is selected as an integer. This approach gives a rigorous definition of the surface topology and allows systematic modification of specific topological parameters to investigate their effects, as opposed to a heuristic method of approximating a braided cable topology. To create a model with added topology, the height variation with  $s$  and  $z$  is superimposed on a nominal cross-sectional shape, such as the one shown in Fig. 1. The baseline cylinder with topology, shown in Fig. 2, has  $\epsilon_o/d = 5\%$ ,  $\lambda_s/d = 0.61$  ( $n = 10$ ) and  $\lambda_z/\lambda_s = 1.5$ , and approximates the geometry of 600 lb load-capacity Dacron cable. The effect of surface height amplitude is investigated using a second cylinder with a higher amplitude of  $\epsilon_o/d = 10\%$  and the same  $\lambda_s$  and  $\lambda_z$ . The effect of topology wavelength is investigated using a cylinder with  $\epsilon_o/d = 5\%$  and a smaller wavelength of  $\lambda_s/d = 0.31$  ( $n = 20$ ). The baseline cylinder without topology ( $\epsilon_o/d = 0$ ) is machined from aluminum, while the cylinders with topology consist of a 3D printed plastic outer sleeve around a solid aluminum spar. The solid aluminum spar corrects any warping or twisting in the 3D printed parts and maintains spanwise straightness over time. The geometric parameters of the four models used in this study are summarized in Table 1.

The models have dimensions  $d = 20$  mm and  $l = 320$  mm, which spans the height of the test section between circular end plates. The end plates are fixed to the tunnel walls and have a diameter of  $15d$  and a  $30^\circ$  chamfered edge. In addition to the large end plates, small end plates with  $4.5d$  diameter and 0.75 mm thickness were fixed to the ends of the model. These small end plates were necessary to eliminate axial flow effects due to air being drawn into the test section from the surroundings through the  $20$  mm  $\times$   $30$  mm holes in the end plates. The hole in the upper end plates allows the model support shaft to pass through the end plate to connect with a force balance while moving freely. The nominal solid blockage of the models at  $\alpha = 0^\circ$  is 5%.

The accuracy of the 3D printed topology models is assessed prior to the wind tunnel experiments to ensure that the intended surface

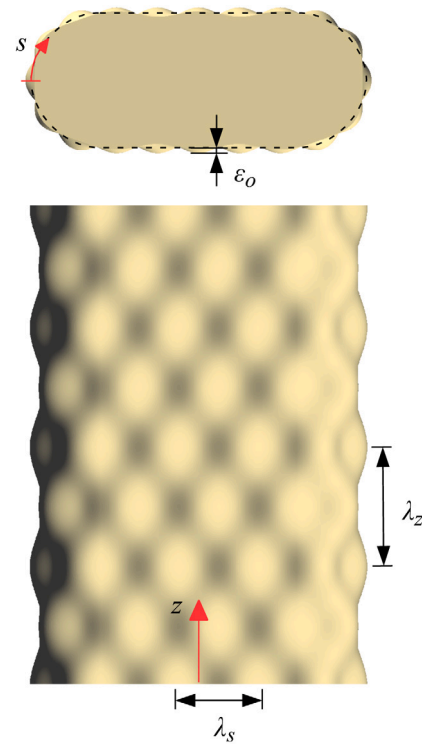


Fig. 2. Top and side views of the cylinder with  $\epsilon_o/d = 5\%$ ,  $\lambda_s/d = 0.61$  and  $\lambda_z/\lambda_s = 1.5$ . The dashed line indicates the nominal smooth cylinder.

height variation is faithfully reproduced. The surface height variation is measured using a Keyence VR 3200 3D profilometer over a 18 mm by 24 mm area centered at the model centerline (i.e.,  $z = 0$  and  $s = 0$ ). Note that due to the length of the model, the 3D printed sleeve is manufactured in two spanwise segments that meet at the midspan of the model ( $z = 0$ ). Fig. 3 shows a comparison of the theoretical to the measured  $\epsilon/\epsilon_o$  for the  $\epsilon_o/d = 5\%$  (equivalent to  $\epsilon_o = 1$  mm),  $\lambda_s/d = 0.61$  model. The results in Fig. 3 demonstrate that despite some slight distortion near  $z = 0$  where the two model halves meet, the 3D printed model accurately reproduces the prescribed surface topology. A measurement of  $\epsilon/\epsilon_o$  along the leading edge (not shown for brevity) shows similar agreement between the nominal and the measured surface height.

Mean lift and drag forces on the models are measured using a custom designed one-component force balance (Feero et al., 2019). This force balance is designed to allow accurate load measurement despite the low Reynolds number range where commercially available load cells would be inadequate. To give a sense of scale, a drag coefficient  $C_D = 1$  for the models used in this study corresponds to a drag force ranging from approximately 2.5 to 200 mN over  $Re_d = 1100$  to 10,000. The force balance is comprised of a four bar parallelogram linkage from which the model is vertically suspended. A horizontal aerodynamic force on the model causes the linkage/model to displace primarily in the horizontal direction, and this displacement is measured by a non-contact laser displacement sensor. Given the stiffness of the force balance, which depends on model weight, it provides a resolution of 0.19 mN. For  $C_D$  or  $C_L$  of 1, the typical accuracy of the force measurements ranges from 0.2 mN to 2.3 mN over  $Re_d = 1100$  to 10,000. Forces were measured for a range of  $\alpha$ , where the model angle was varied using a step-servo motor with a resolution of  $0.02^\circ$ . The  $0^\circ$  angle-of-attack position was determined by adjusting the model angle until symmetry was achieved in the force being measured (either lift or drag). The entire force balance can be rotated to switch between lift and drag measurement. Further details concerning the experimental setup and procedure can found in Feero et al. (2019, 2020), which focused on investigating smooth models.



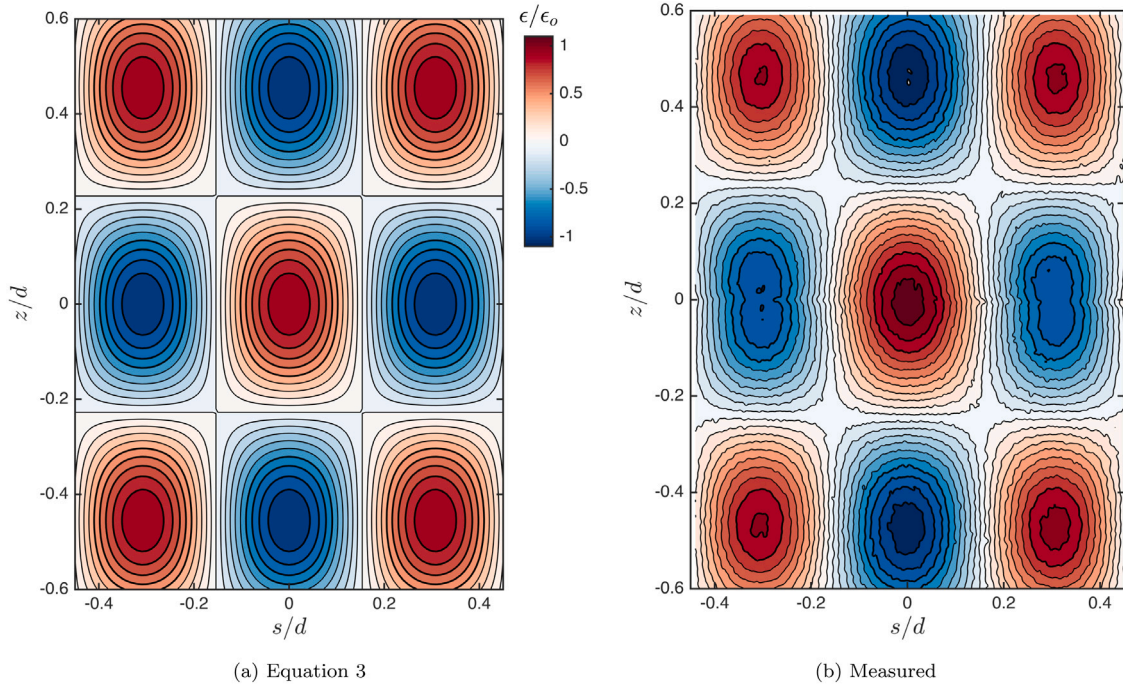


Fig. 3. Comparison between theoretical and measured  $\epsilon/\epsilon_o$  for the  $\epsilon_o/d = 5\%$ ,  $\lambda_s/d = 0.61$ ,  $\lambda_z/\lambda_s = 1.5$  model. Note that equivalent contour levels are used in the two plots.

### 3. Results

#### 3.1. Topology amplitude

This section is focused on discussing the effects of topology amplitude,  $\epsilon_o$ , for a fixed  $s$ -direction wavelength of  $\lambda_s/d = 0.61$  (equivalent to  $n = 10$ ). The lift and drag forces are measured for  $-5^\circ \leq \alpha \leq 15^\circ$  at  $Re_d = 1100, 2500, 5000, 7500$  and  $10,000$  for each of the models. Results at  $Re_d = 1100$  and  $Re_d = 10,000$  are shown in Fig. 4. For the smooth model at  $Re_d = 10,000$ ,  $C_L$  varies with  $\alpha$  in a way that is similar to a streamlined body; that is,  $C_L$  increases as  $\alpha$  increases from  $0^\circ$  up to a maximum at  $3^\circ$  and then experiences a moderate decrease. A second peak occurs in  $C_L$  at  $\alpha = 6^\circ$ , which is followed by  $C_L$  increasing slightly with  $\alpha$ . The  $\epsilon_o/d = 5\%$  model displays a similar trend, although the maximum  $C_L$  is reduced relative to the smooth case. This case also exhibits some asymmetry between positive and negative angles of attack, the reason for which is unknown. As the surface height amplitude increases to  $\epsilon_o/d = 10\%$ , no peaks in  $C_L$  are observed but rather the slope of  $C_L$  smoothly decreases and the curve approximately plateaus at  $6^\circ$ . For small values of  $\alpha$ , below that of the first peak and the plateau, the slope of the lift curve decreases with increasing topology amplitude.

A considerable change in the overall behavior in  $C_L$  is observed for all geometries when  $Re_d$  is reduced to 1100. At this Reynolds number, the slope in  $C_L$  near  $\alpha = 0^\circ$  is negative for all but the smooth case. The peak  $C_L$  magnitude is decreased substantially to approximately 0.2, whereas values up to 1.2 occur at  $Re_d = 10,000$ . Unlike the topology models, the smooth model experiences a nearly linear increase with  $\alpha$  over the entire range.

The drag coefficient at  $Re_d = 1100$  and  $10,000$  is shown in Fig. 4c and d, respectively. Examining first the smooth geometry at  $Re_d = 10,000$ ,  $C_D$  is found to decrease slightly as  $\alpha$  increases from  $0^\circ$  to  $2^\circ$ , beyond which it increases monotonically with  $\alpha$ . Over  $0^\circ \leq \alpha \leq 15^\circ$ ,  $C_D$  increases by more than a factor of two from approximately 0.5 to 1.2. When the  $\epsilon_o/d = 5\%$  surface topology is added, the slope of  $C_D$  becomes exclusively positive over the entire  $\alpha$  range (except at  $\alpha = 0^\circ$  where the slope is approximately zero), and there is a small increase in  $C_D$  relative to the smooth case at  $\alpha = 0^\circ$ . As  $\epsilon_o/d$  increases from 5%

to 10%, the  $C_D$  curve near  $\alpha = 0^\circ$  becomes substantially flatter and  $C_D$  at  $\alpha = 0^\circ$  increases from 0.6 to 0.8. Unlike  $C_L$ , when  $Re_d$  decreases to 1100 there is not a reversal in the qualitative behavior of  $C_D$ . All the geometries maintain a slope in  $C_D$  that is approximately zero or positive over the  $\alpha$  range. The  $\epsilon_o/d = 5\%$  and  $\epsilon_o/d = 10\%$   $C_D$  curves are equivalent within the uncertainty and are flatter than the smooth case near  $\alpha = 0^\circ$ .

The normal force coefficient,  $C_y$ , is computed from  $C_D$  and  $C_L$  according to Eq. (1). The variation in  $C_y$  with  $\alpha$  for the entire Reynolds number range is shown in Fig. 5 for each geometry. The solid lines in these plots are curve fits computed using either a cubic spline or a sliding cubic fit to smooth scatter in the data, where the latter case is typically used for  $Re_d < 5000$ . Comparing the results at  $Re_d = 1100$  and  $10,000$  to Fig. 4, it can be observed that  $C_y$  follows a trend quite similar to  $-C_L$ . Examining first the results for the smooth geometry in Fig. 5a, the slope in  $C_y$  is negative at small angles-of-attack for all  $Re_d$ . This slope becomes increasingly negative as  $Re_d$  increases from 1100 to 5000, after which it begins to decrease in magnitude while remaining negative. Recall from the introduction that a body is unstable with respect to galloping when  $\partial C_y/\partial \alpha$  is positive. As  $Re_d$  increases above 1100, a minimum in  $C_y$  begins to emerge near  $\alpha \approx 3^\circ$ , with the value of this minimum reaching peak magnitude at  $Re_d = 5000 - 7500$  before decreasing at  $Re_d = 10,000$ . The double peak behavior that was observed in  $C_L$  for  $Re_d = 10,000$  remains present in  $C_y$  as double minima at approximately  $3^\circ$  and  $6^\circ$ . For  $Re_d \geq 5000$ ,  $C_y$  shows very little variation with  $Re_d$  at angles-of-attack above approximately  $10^\circ$ .

Fig. 5b shows the  $C_y$  results for the  $\epsilon_o/d = 5\%$  geometry. The addition of this surface topology leads to an initially positive slope in  $C_y$  at  $Re_d = 1100$ , and therefore a geometry that is unstable in the transverse galloping mode. As  $\alpha$  increases,  $C_y$  reaches a peak after which the slope becomes approximately constant and negative. A transition occurs between  $Re_d = 1100$  and  $2500$ , as  $\partial C_y/\partial \alpha$  at  $\alpha = 0^\circ$  becomes negative, indicating stability. For  $Re_d \geq 2500$ , the shape in  $C_y$  is similar to that of the smooth geometry, however the magnitude of the  $C_y$  minimum is reduced. The effect of  $Re_d$  on this minimum magnitude is less than what is seen for the smooth case. A double minima behavior in  $C_y$ , as was observed for the smooth case at  $Re_d = 10,000$ , occurs for

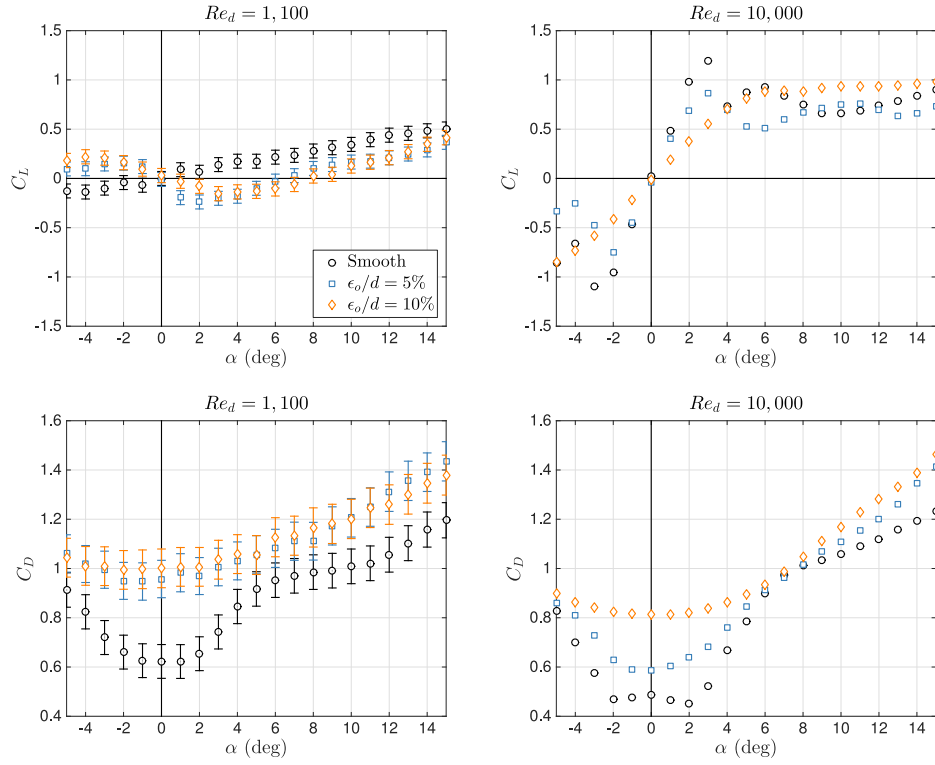


**Fig. 4.** Lift and drag coefficient variation with angle-of-attack for the smooth and topology models with  $\epsilon_o/d = 5\%$  and  $\epsilon_o/d = 10\%$  ( $\lambda_s/d = 0.61$ ). For  $Re_d = 10,000$ , error bars are less than the marker size.

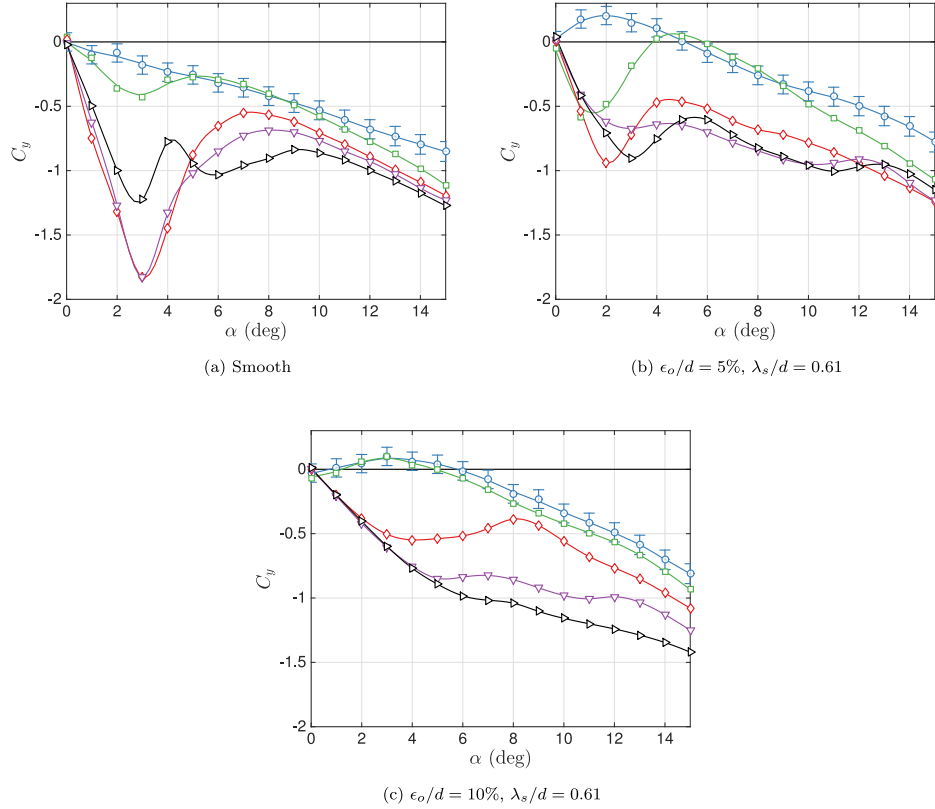


**Fig. 5.** Reynolds number effect on  $C_y$  versus  $\alpha$ . Solid lines are curve fits to the data. Error bars are less than the marker size for  $Re_d \geq 2500$ . ( $\circ$ )  $Re_d = 1100$ , ( $\square$ ) 2500, ( $\diamond$ ) 5000, ( $\nabla$ ) 7500, ( $\triangleright$ ) 10,000.

the  $\epsilon_o/d = 5\%$  geometry for  $Re_d \geq 7500$ , with the second minimum occurring at a larger  $\alpha$  relative to the smooth case.

The effect of the largest topology amplitude  $\epsilon_o/d = 10\%$  on  $C_y$  is shown in Fig. 5c. For  $Re_d \leq 2500$ , the shape of  $C_y$  is similar to that of

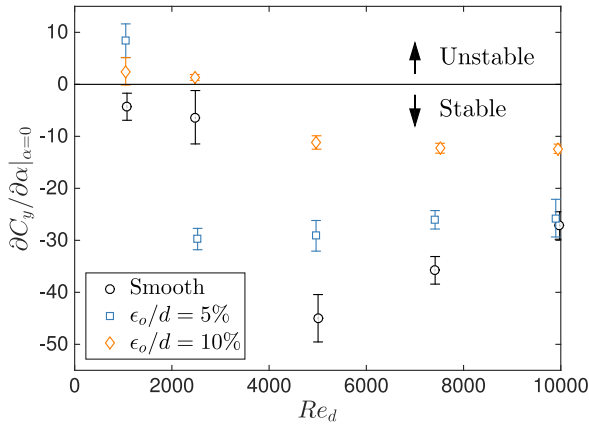


Fig. 6. Effect of the topology amplitude for  $\lambda_s/d = 0.61$  on the galloping criterion at  $\alpha = 0^\circ$  with comparison to the smooth geometry.

$Re_d = 1100$  for  $\epsilon_o/d = 5\%$ , although the magnitude of the maximum is decreased and it occurs at a slightly larger  $\alpha$ . However, for  $Re_d \geq 5000$ ,  $C_y$  is distinctly different from both the smooth and  $\epsilon_o/d = 5\%$  cases. At  $Re_d = 5000$ , a minimum in  $C_y$  is still observed, but  $C_y$  is substantially flatter at angles-of-attack near the minimum. Increasing  $Re_d$  from 5000 to 10,000 results in a disappearance of this minimum, and a transition to  $C_y$  that is constantly decreasing with increasing  $\alpha$  at  $Re_d = 10,000$ . Unlike the other two geometries,  $\epsilon_o/d = 10\%$  shows a noticeable Reynolds number effect on  $C_y$  at large angle-of-attack, where the magnitude of  $C_y$  increases monotonically with increasing  $Re_d$ .

Fig. 6 shows the effect of  $\epsilon_o/d$  on the galloping criterion evaluated at  $\alpha = 0^\circ$ ,  $\partial C_y/\partial \alpha|_{\alpha=0}$ , over the entire Reynolds number range. The derivative  $\partial C_y/\partial \alpha$  is evaluated from the curve fits of  $C_y(\alpha)$  described previously. The uncertainty in  $\partial C_y/\partial \alpha$  is computed using a Monte Carlo method with  $5 \times 10^3$  random samples, as described in the Appendix. For the smooth cylinder,  $\partial C_y/\partial \alpha|_{\alpha=0} < 0$  and thus this geometry is stable with respect to galloping over  $1100 \leq Re_d \leq 10,000$ . As  $Re_d$  decreases from 10,000 to 5000,  $\partial C_y/\partial \alpha|_{\alpha=0}$  becomes increasingly negative, however a dramatic increase occurs when  $Re_d$  decreases to 2500. Although the value of  $\partial C_y/\partial \alpha|_{\alpha=0}$  remains negative, it becomes substantially closer to the instability threshold for  $Re_d \leq 2500$  compared with higher Reynolds number. The addition of the  $\epsilon_o/d = 5\%$  topology generally causes  $\partial C_y/\partial \alpha|_{\alpha=0}$  to increase relative to the smooth case, indicating that this topology is generally destabilizing. This is particularly true at  $Re_d = 1100$ , where  $\partial C_y/\partial \alpha|_{\alpha=0} > 0$  and the geometry is unstable. For  $Re_d \geq 5000$ ,  $\partial C_y/\partial \alpha|_{\alpha=0}$  increases relative to the smooth case but does not become positive. Increasing  $\epsilon_o/d$  to 10% generally has the same effect as  $\epsilon_o/d = 5\%$ , except the larger amplitude makes the magnitude of  $\partial C_y/\partial \alpha|_{\alpha=0}$  smaller. As a result, the increase in  $\epsilon_o/d$  becomes destabilizing for  $Re_d \geq 5000$ , since it causes the derivative to move closer to the instability threshold. On the other hand, for  $Re_d = 1100$ , while the larger amplitude also makes the cylinder unstable, the decrease in the derivative magnitude makes the cylinder less prone to vibration since a larger critical reduced velocity would be required for the onset of oscillation. For all cases, the qualitatively different behavior between  $Re_d = 1100$  and  $Re_d \geq 5000$  is indicative of a transitional  $Re_d$  range that seems to encompass  $Re_d = 2500$ . This may explain the lack of systematic trends for measurements at this Reynolds number. This includes the large change in  $\partial C_y/\partial \alpha|_{\alpha=0}$  at  $Re_d = 2500$  and a behavior of the derivative with  $\epsilon_o/d$  that is different from the low ( $Re_d = 1100$ ) and high ( $Re_d \geq 5000$ ) Reynolds number cases.

The previous discussion regarding galloping stability was based on the value of  $\partial C_y/\partial \alpha|_{\alpha=0}$ , where  $\partial C_y/\partial \alpha|_{\alpha=0} > 0$  indicates a body that would gallop from rest. In this case, if the reduced velocity is higher than the critical value, any small disturbance that causes an initial motion of the body will lead to oscillations that increase in time until

non-linearities in the structure and/or fluid force drive the system toward a stable limit cycle of oscillations (Barrero-Gil et al., 2009). However, for cases where  $\partial C_y/\partial \alpha|_{\alpha=0} < 0$ , the body may still be prone to galloping in a hard oscillation mode. This can occur if there are ranges of  $\alpha$  away from  $0^\circ$  where  $\partial C_y/\partial \alpha > 0$ . Unlike “soft” oscillators, a hard oscillator requires a large initial disturbance to reach the basin of attraction of the limit cycle (Novak, 1972). The results in Fig. 5 demonstrate for all three geometries, regions of  $\partial C_y/\partial \alpha > 0$  exist for Reynolds numbers where  $\partial C_y/\partial \alpha|_{\alpha=0} < 0$ . The hard galloping behavior of each geometry is considered by examining  $\partial C_y/\partial \alpha$  as a function of  $\alpha$ , as shown in Fig. 7. Results are shown at  $Re_d = 5000$  and 10,000, since each geometry is stable to galloping from rest, i.e., at  $\alpha = 0^\circ$ , over this Reynolds numbers range (Fig. 6).

At  $Re_d = 5000$ ,  $\partial C_y/\partial \alpha$  for the smooth geometry is initially negative but becomes positive for  $\alpha$  between approximately  $3^\circ$  and  $7^\circ$ . The angle where  $\partial C_y/\partial \alpha$  first becomes positive (i.e.,  $3^\circ$  for the smooth case) will be referred to as the galloping angle. The presence of the surface topology with  $\epsilon_o/d = 5\%$  results in a reduction in the galloping angle to approximately  $2^\circ$ . Therefore, the  $\epsilon_o/d = 5\%$  topology at  $Re_d = 5000$  makes the geometry more susceptible to hard galloping, as a smaller galloping angle corresponds to a smaller initial disturbance being capable to initiate oscillation. Increasing  $\epsilon_o/d$  to 10% results in an increase in the galloping angle relative to the smooth case, and also much smaller positive  $\partial C_y/\partial \alpha$  magnitude. It is interesting to note that for  $\alpha > 8^\circ$ , surface topology has no effect on the slope of  $C_y$  as all three cases essentially collapse.

The effect of topology on  $\partial C_y/\partial \alpha$  at  $Re_d = 10,000$  is shown in Fig. 7b. Unlike at  $Re_d = 5000$ , the addition of surface topology does not make the body more susceptible to hard galloping relative to the smooth case. The  $\epsilon_o/d = 5\%$  topology has essentially the same galloping angle of  $\sim 3^\circ$  as the smooth case. The large amplitude topology,  $\epsilon_o/d = 10\%$ , at  $Re_d = 10,000$  is an interesting case as it is completely stable over the investigated  $\alpha$  range and is not susceptible to hard galloping. This is contrary to the destabilizing effect that increasing  $\epsilon_o/d$  to 10% has on soft galloping. Although not shown for brevity, this was also the case for the  $\epsilon_o/d = 10\%$  geometry at  $Re_d = 7500$ . A consistent trend over  $5000 \leq Re_d \leq 10,000$  is that the addition of surface topology leads to a decrease in the peak positive value of  $\partial C_y/\partial \alpha$  relative to the smooth case (or the elimination of positive  $\partial C_y/\partial \alpha$  altogether). For a given elastically mounted body, a decrease in the magnitude of positive  $\partial C_y/\partial \alpha$  is associated with a decrease in the amplitude of oscillation and an increase in the critical reduced velocity required for galloping to occur (Blevins, 2001). The results at  $Re_d = 10,000$  also show that unlike  $Re_d = 5000$ , there are two ranges of  $\alpha$  where the slope of  $C_y$  is positive for  $\epsilon_o/d < 10\%$ . This is associated with the double peak behavior observed in Fig. 5 for certain  $Re_d$ .

### 3.2. Topology wavelength

The effect of topology wavelength is considered by comparing the  $C_y$  behavior of the  $\lambda_s/d = 0.61$  and  $\lambda_s/d = 0.31$  cylinders, which have the same amplitude of  $\epsilon_o/d = 5\%$ . The normal force coefficient variation with angle-of-attack for these two geometries is shown in Fig. 8, where the solid and dashed lines represent  $\lambda_s/d = 0.61$  and  $\lambda_s/d = 0.31$ , respectively. The results are presented in two different plots with different Reynolds number ranges to highlight the observation that in the regime  $Re_d \leq 5000$ , there is almost no effect in changing topology wavelength on  $C_y$ . This is particularly true for the slope of  $C_y$  at  $\alpha = 0^\circ$ , which is equivalent within experimental uncertainties. Some effect of topology wavelength is observed for  $Re_d = 5000$  where the local maximum in  $C_y$  decreases in magnitude and shifts to a larger angle-of-attack with decreasing wavelength. For the larger Reynolds number range ( $Re_d > 5000$ ), the force characteristics are influenced by  $\lambda_s$ , however the influence does not alter  $\partial C_y/\partial \alpha|_{\alpha=0}$  considerably. The  $C_y$  slope at  $\alpha = 0^\circ$  increases slightly with decreasing  $\lambda_s$  but remains strongly negative and therefore stable. A consistent feature in this

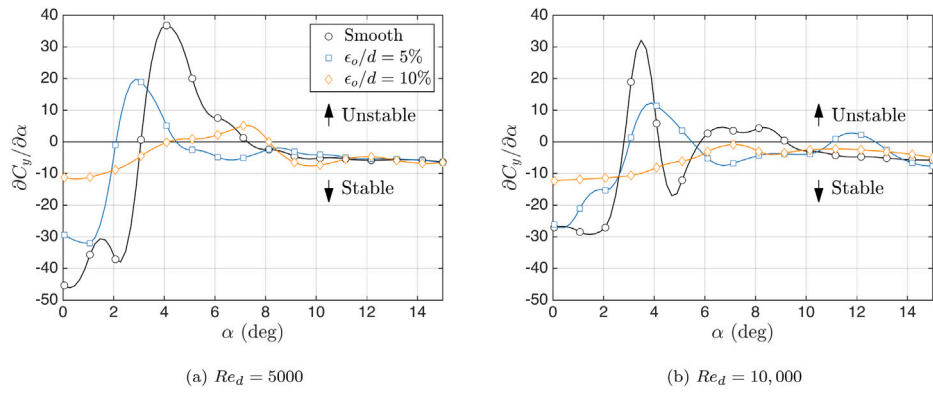


Fig. 7. Normal-force coefficient derivative variation with angle-of-attack for the smooth cylinder, and topology cylinders with  $\lambda_s/d = 0.61$ .

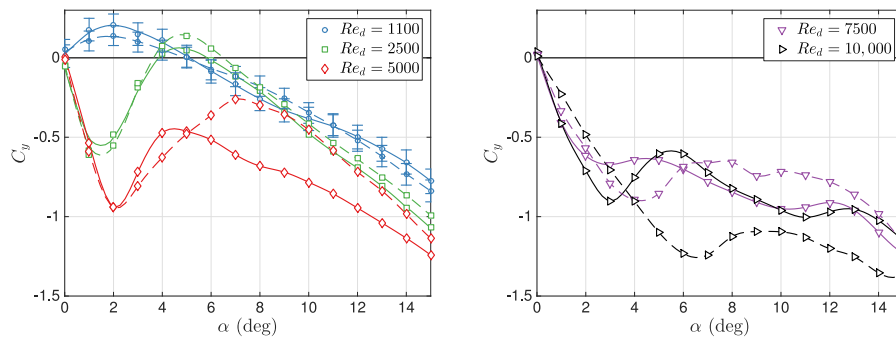


Fig. 8. Effect of topology wavelength on the normal force coefficient variation with angle-of-attack for  $\epsilon_o/d = 5\%$ . Solid and dashed lines indicate  $\lambda_s/d = 0.61$  and  $\lambda_s/d = 0.31$ , respectively.

Reynolds number range is the decrease in the local  $C_y$  minimum with decreasing wavelength, and an associated shift in this minimum to a larger  $\alpha$  (e.g., from  $\alpha = 3^\circ$  to  $\alpha \approx 7^\circ$  at  $Re_d = 10,000$ ). This implies an increase in the angle at which the model could become prone to hard galloping. In general, however, over the ranges of  $\epsilon_o$  and  $\lambda_s$  investigated in this study, changing topology amplitude is found to have a more pronounced influence on altering the cylinder's force characteristics than changing topology wavelength.

#### 4. Discussion

The literature review in Section 1 shows that for sharp-cornered rectangles, stability to galloping (specifically whether  $C_y$  decreases or increases with  $\alpha$ ) primarily depends on whether the separating shear layer on the bottom side of the cylinder reattaches, and if the resulting separation bubble shrinks with increasing angle of attack. For cylinders that are unstable to galloping, the shear layer on the top side of the cylinder remains separated with increasing  $\alpha$ , and hence boundary layer reattachment on the top does not play a role in galloping stability. The present cylinder models, however, have a baseline geometry with fully-round corners ( $r/d = 0.5$ ), and while there is very little information on this geometry in literature, from what is available, we reason that the  $C_y - \alpha$  characteristics, and hence the galloping stability, of the present geometry is controlled by the behavior of the shear layer on the top side of the cylinder. The following discussion clarifies the bases for this hypothesis.

To appreciate the fundamental effect that corner rounding can have on galloping instability, consider the study of Carassale et al. (2014). In their study of square cylinders with sharp corner,  $r/d = 0.067$  and  $r/d = 0.133$ , Carassale et al. (2014) showed that, in a freestream with 5% turbulence intensity, the largest corner radius causes the separating shear layer on top of the cylinder to have a significant influence on the lift coefficient variation with angle of attack ( $C_L \approx$

$-C_y$  at small values of  $\alpha$ ), above a certain critical Reynolds number ( $Re_d \approx 10^5$ ). Specifically, at supercritical conditions, the  $C_L - \alpha$  slope becomes positive, indicating stability to galloping, and  $C_L$  increases to a maximum before decaying with further increase in  $\alpha$ . Similar supercritical behavior was not observed for the sharp- and smaller-corner-radius cylinders. The flip in the sign of  $\partial C_y / \partial \alpha|_{\alpha=0}$  between subcritical and supercritical conditions was found to be connected to the shear layers ability to reattach on the sides of the cylinder at  $\alpha = 0^\circ$  for supercritical conditions and the largest corner radius. The reattachment occurs notwithstanding the very short afterbody of the  $c/d = 1$  geometry. As  $\alpha$  increases, the separation bubble on the bottom side shrinks in size, leading to increased pressure on the bottom, and hence increasing  $C_L$ . Simultaneously, the separation bubble on the top side remains closed, exerting suction pressure that increases in magnitude with  $\alpha$  on the upper front corner and the top surface. This contributes further to the increase of  $C_L$  with  $\alpha$ , which leads to galloping stability. Beyond a certain angle of attack, the bubble on the top side starts to lengthen significantly with increasing  $\alpha$ , and the corner pressure starts to increase. This corresponds to the maximum  $C_L$  and the subsequent decay of  $C_L$  with  $\alpha$ . Eventually, with additional increase in  $\alpha$ , an open separation forms on the top side and the flow becomes similar to that at subcritical conditions. At this point, the  $C_L - \alpha$  curves for sub and supercritical conditions collapse.

The work of Carassale et al. (2014) highlights the fact that corner rounding can make boundary layer separation and reattachment on the top side of the cylinder significant to galloping stability of rectangular sections. In the present study, the baseline geometry has a fully-round corner (i.e., a semi-circular leading edge), which is much more of an "aerodynamic" shape than that of the cylinder with the largest corner radius used by Carassale et al. (2014). With such significant rounding, it is not known if the boundary layer would separate over the corner, as is the case for the sharp and small-radius corners. Kalan et al. (2020) recently examined the boundary layer characteristics over the



top surface of the present study's smooth and 5%-topology cylinder geometry at  $Re_d = 2500$  in a water tunnel. Using measurements at  $\alpha = 0^\circ, 2^\circ$ , and  $5^\circ$ , they found separation to start some distance downstream of the corner, on the flat side of the smooth-surface cylinder. This judgment was made based on identifying the boundary of the reversed-flow region; although the study did not have sufficient resolution to accurately determine the precise location of separation. Kalan et al. (2021) observed the same behavior on the top side of the cylinder at a lower Reynolds number of 1100. In addition, they found that no separation takes place on the bottom side of the smooth cylinder for the same  $\alpha$  values examined in Kalan et al. (2020) for  $Re_d = 1100$  and 2500. With the absence of leading-edge (LE) separation, and the flow staying attached on the cylinder's bottom surface, the smooth cylinder behaves more like a lifting body, albeit an inefficient one. This is the likely reason why this geometry remains stable to galloping in the Reynolds number range of concern,  $Re_d = 1000 - 10,000$ , as seen in Fig. 5a.

For the case with topology, Kalan et al. (2021) conducted measurements in two different spanwise planes: one aligned with a topology peak at the leading edge, and the other with a topology valley. The authors found only a thin, localized separation bubble on the bottom side of these cylinders. This suggests that even in the presence of topology, boundary layer separation and reattachment on the bottom surface is likely insignificant to the galloping stability of the cylinders. This leaves the change in separation and reattachment behavior on the top surface of the cylinder as the probable cause for the cylinders becoming unstable to galloping when the Reynolds number is sufficiently low (Fig. 5).

The data in Kalan et al. (2020) show that while separation occurs downstream of the corner on the top surface when a topology valley is present at the leading edge, the presence of a peak at the leading edge causes the shear layer to separate somewhere along the corner region. In other words, the biggest influence of the topology seems to be in promoting LE separation on the top surface when a topology peak is at the LE. At the higher  $Re_d$  of 2500, the shear layer seems to reattach on the side of the cylinder at  $\alpha = 0^\circ$  and  $2^\circ$ , but the separation bubble is open at  $\alpha = 5^\circ$  (Kalan et al., 2020). This behavior of a leading edge separated shear layer that reattaches on the upper cylinder side, becomes longer with increasing angle of attack, and eventually detaches from the surface is similar to the supercritical behavior seen in Carassale et al. (2014), which leads to stability to galloping. This apparent transition to what Carassale et al. call supercritical state at a significantly lower Reynolds number might be linked to the milder curvature of the corner ( $r/d = 0.5$  versus 0.133 for Carassale et al.), and the longer afterbody ( $c/d = 2.5$  versus 1) of the present study.

As the Reynolds number decreases from 2500 to 1100, Kalan et al. (2021) found that, in the spanwise plane where a topology peak is at the leading edge, while separation still occurs somewhere along the corner, there is no evidence of reattachment on the top side of the cylinder. The absence of reattachment is akin to the flow behavior of the sharp- and small-radius-corner cylinders in Carassale et al. (2014), which was associated with instability to galloping. It is important to note that in using Kalan et al.'s (2020, 2021) measurements in a water tunnel to interpret the present measurements in a wind tunnel, we primarily make use of trends in Reynolds number variation, rather than assuming the same force characteristics of the same model geometry at the same Reynolds number. Such similarity would require matching of other parameters with important influence on the problem, including the freestream turbulence intensity, the model's aspect ratio, and the tunnel blockage, which are not matched between the two studies.

The above discussion leads to the hypothesis that the destabilizing effect of topology is driven by earlier separation around the front top corner of the model at cross sections where the topology causes the surface to protrude further into the flow relative to the baseline smooth geometry. For a sufficiently high Reynolds number ( $Re_d \geq 2500$  for  $\epsilon_o/d = 5\%$ , and  $Re_d \geq 5000$   $\epsilon_o/d = 10\%$ ), the separated shear layer is able to reattach on the side of the cylinder over a certain range

of  $\alpha$ , leading to stability to galloping. At lower Reynolds number, the separation remains open and the geometry is unstable to galloping. While at other cross sections along the span (where a topology valley is present at the LE) separation occurs downstream of the corner, it appears that on average the earlier separation has a stronger influence. To understand why this is the case, and if indeed the hypothesis is correct, it is necessary to conduct more boundary layer measurements at several Reynolds numbers, along with force measurements. These studies are underway.

Another interesting effect in Fig. 5 is the weakening, and even disappearance at  $Re_d = 10,000$ , of the local minimum in the  $C_y - \alpha$  as the topology amplitude is increased from 5% to 10%. This effect is favorable from the perspective of hard galloping (in fact leading to complete stability to hard galloping at  $Re_d = 10,000$  when  $\epsilon_o/d = 10\%$ ; Fig. 7). This behavior is reminiscent of observations of  $C_L - \alpha$  (recall  $C_L \approx -C_y$ ) for airfoils with sinusoidally-shaped leading edge. Such airfoils are typically studied to understand the aerodynamic benefits of tubercles, which are protuberances that are found on the flippers of humpback whales. Most of the studies on this topic pertain to high Reynolds numbers with the lowest Reynolds number data found in Hansen et al. (2011), considering a NACA 0021 airfoil at Reynolds number based on chord of 120,000. These results are consistent with the literature in showing that the abrupt drop in the maximum lift coefficient past stall is replaced by a much smoother stall peak in the presence of the protuberances and a smaller maximum lift coefficient. Increasing the amplitude of the protuberances leads to the stall becoming less prominent. Moreover, Hansen et al. (2011) also investigated the effect of changing the wavelength of the protuberances. The results show that decreasing the wavelength leads to increasing the maximum lift and the stall angle.

The effect of the amplitude of the leading-edge protuberances on the stall peak of the NACA 0021 airfoil is qualitatively consistent with the results in Fig. 5b and c, for  $Re_d \geq 5000$ , which according to the conjectures developed earlier in this section, exhibit supercritical conditions, and hence behave as a lifting body. Similarly, the results in Fig. 8 do show delayed stall angle and a larger maximum lift coefficient (recall  $C_L \approx -C_y$ ) with decreasing topology wavelength for  $Re_d = 7500$  and 10,000. These observations suggest that the present surface topology may, in large part, behave as airfoil leading-edge protuberances if the Reynolds number is sufficiently high. Present understanding of the effect of protuberances on airfoil performance is that they generate streamwise vortices, which lead to desirable enhancement in the airfoils stall characteristics (see Hansen et al., 2011 and references therein) while not influencing the lift behavior at small angles of attack. One would expect the effectiveness of such vortex-generators to depend on the size of the vortices relative to the boundary layer thickness, and hence Reynolds number. From the perspective of the present investigation, if indeed the surface topology leads to streamwise vortex generation at the leading edge, the effect is relevant to the higher Reynolds number range, where the cylinders are stable to soft, but unstable to hard galloping. The latter is connected directly with the presence and prominence of the "stall" peak.

Given that the motivating application of the present study is in air, this work has focused on understanding the stability to galloping from the perspective of quasi-steady conditions. This perspective is based on the expected much lower frequency of galloping oscillation compared to that of vortex shedding. While this is the established knowledge in literature, we do recognize that within the unique geometry and Reynolds number range of the present work, other time scales, aside from that of vortex shedding, may arise and cause the invalidity of quasi-steadiness. More specifically, time scales associated with separation and reattachment behavior that are different from those at higher Reynolds numbers might lead to such invalidity. A separate study, which is outside the scope of the present investigation, is presently being planned to investigate the limits of quasi-steadiness.



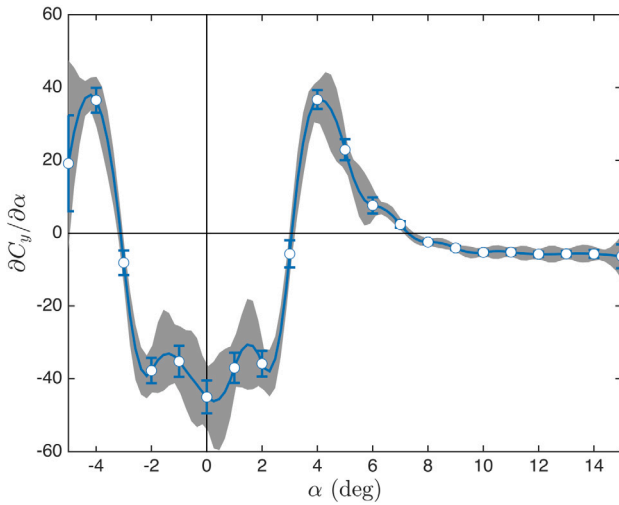


Fig. 9. Example  $\partial C_y/\partial \alpha$  variation with  $\alpha$  and uncertainty indicated with error bars. The shaded region indicates the range of  $\partial \widetilde{C}_y/\partial \alpha$  for  $N = 5000$ .

## 5. Conclusions

The effect of surface topology amplitude and wavelength on the galloping instability of a rectangular cylinder with side ratio  $c/d = 2.5$  and corner radius  $r/d = 0.5$  was investigated experimentally for Reynolds numbers  $Re_d = 1100 - 10,000$ . Two topology amplitudes were tested,  $\epsilon_o/d = 5\%$  and  $10\%$ , at a constant  $\lambda_s/d = 0.61$ . Similarly, two wavelengths along the perimeter ( $s$ -direction) were tested,  $\lambda_s/d = 0.61$  and  $0.31$ , with constant  $\epsilon_o/d = 5\%$ . For all cylinders with topology, the spanwise-to-perimeter wavelength ratio was held fixed at  $\lambda_z/\lambda_s = 1.5$ .

The smooth geometry showed a lift curve with positive slope near angle-of-attack  $\alpha = 0^\circ$  over the entire  $Re_d$  range, while the added topology led to a shift from positive to negative slope with decreasing  $Re_d$ . The topology was found to increase drag at  $\alpha = 0^\circ$  relative to the smooth case, with the increase being constant at  $Re_d = 1100$  and monotonically increasing with  $\epsilon_o/d$  at  $Re_d = 10,000$ .

The smooth geometry was found to be stable to galloping over the investigated Reynolds number range, as indicated by  $\partial C_y/\partial \alpha|_{\alpha=0} < 0$  (where  $C_y$  is the force coefficient in the galloping direction). In general, the results showed that the addition of surface topology had a destabilizing effect and caused an increase in  $\partial C_y/\partial \alpha|_{\alpha=0}$ . This increase lead to instability ( $\partial C_y/\partial \alpha|_{\alpha=0} > 0$ ) for each topology geometry at  $Re_d = 1100$ . In addition to the stability criterion for galloping from rest,  $\partial C_y/\partial \alpha|_{\alpha=0}$ , the hard galloping behavior was also investigated. With the exception of the  $\epsilon_o/d = 10\%$  geometry at high Reynolds number, all of the geometries showed susceptibility to hard galloping in cases where they were stable to galloping from a small disturbance. Increasing  $\epsilon_o/d$  was found to decrease or eliminate the susceptibility to hard galloping. This feature along with a smaller magnitude of  $\partial C_y/\partial \alpha|_{\alpha=0}$  renders the  $10\%$  more preferable to the  $5\%$  topology amplitude from the perspective of susceptibility to galloping, irrespective of the initiating disturbance level. The  $s$ -direction wavelength,  $\lambda_s$ , was found to have a comparatively smaller effect than amplitude on the galloping behavior of the cylinder. Varying  $\lambda_s$  had no effect on  $\partial C_y/\partial \alpha|_{\alpha=0}$  for  $Re_d \leq 5000$ , and only a slight decrease in  $\partial C_y/\partial \alpha|_{\alpha=0}$  occurred for  $Re_d > 5000$  with decreasing  $\lambda_s$ . For the latter Reynolds number range, decreasing the wavelength also led to an increase in the disturbance level (instantaneous  $\alpha$ ) required to initiate hard galloping.

Analysis of the results leads to the hypothesis that the effect of the surface topology on galloping stability of rectangular cylinders is primarily driven by the topological features along the leading edge (LE). The details of the topology along the sides and in the wake are of secondary importance. Of particular importance is the role of the

leading-edge topology in causing early separation on the top surface of the cylinder when a topology peak is present at the LE, and the possibility of the topology acting as streamwise vortex generators, to delay and flatten the stall peak for geometry that is stable to soft galloping, and hence acting as a lifting body. The former effect is most significant to soft galloping and the latter to hard oscillation. Additional studies incorporating both force and boundary layer measurements are needed to assess the validity of these ideas.

## CRedit authorship contribution statement

**Mark A. Feero:** Methodology, Software, Formal analysis, investigation, Writing - original draft, Writing - review & editing, Visualization. **Ahmed M. Naguib:** conceptualization, Methodology, Resources, Writing - review & editing, Supervision, Funding acquisition. **Manoochehr M. Koochesfahani:** Conceptualization, Methodology, Resources, Supervision, Funding acquisition.

## Declaration of competing interest

The authors declare that they have no known competing financial interests or personal relationships that could have appeared to influence the work reported in this paper.

## Acknowledgments

The authors would like to acknowledge Mr. Kian Kalan who developed the code and methodology for generating 3D solid models of the cylinders with surface topology and also identified the means for measuring the surface topology.

This project is funded through ARO, USA grant number W911NF1710153. The views and conclusions contained in this document are those of the authors and should not be interpreted as representing the official policies, either expressed or implied, of ARO or the U.S. Government. The U.S. Government is authorized to reproduce and distribute reprints for Government purposes notwithstanding any copyright notation herein.

## Appendix. $\partial C_y/\partial \alpha$ Uncertainty

The uncertainty in  $C_y$  is a function of the uncertainties in the parameters from which it is computed; that is,  $e_{C_y} = f(e_{F_D}, e_{F_L}, e_{U_\infty}, e_\alpha)$ . Two primary sources of uncertainty are considered for each of these quantities: sensor accuracy and statistical convergence of the mean (based on the number of independent samples). For  $F_D$  and  $F_L$ , an additional uncertainty that accounts for the asymmetry of the force behavior is also considered. Since the cylinders have cross sections that are symmetric,  $F_D$  and  $F_L$  should be symmetric and anti-symmetric about  $\alpha = 0^\circ$ , respectively. The symmetry uncertainty is computed as, for example,  $|F_L(\alpha)| - |F_L(-\alpha)|$  over  $-5^\circ \leq \alpha \leq 5^\circ$ . The uncertainty in  $C_y$  is computed using the typical Taylor series error propagation methodology applied to Eq. (1).

A different approach employing Monte Carlo simulations is used to compute the uncertainty for  $\partial C_y/\partial \alpha$ , which is computed from a curve fit of  $C_y(\alpha)$ . The curve fitting is accomplished using two different methods (as described in Section 3.1) based on the amount of data scatter. Using the Monte Carlo approach, a random sequence  $\widetilde{C}_y = (\widetilde{C}_{y1}, \dots, \widetilde{C}_{yN})$  is computed, viz.

$$\widetilde{C}_{yi} = C_y + \frac{e_{C_y}}{2} r_i, \quad (4)$$

where  $r$  is a random number drawn from the standard normal distribution and  $N$  is the number of replications. A curve fit of  $\widetilde{C}_{yi}(\alpha)$  is applied for each replication, differentiated to obtain  $\partial \widetilde{C}_{yi}/\partial \alpha$ , and finally the uncertainty in  $\partial C_y/\partial \alpha$  at the 95% confidence interval is computed as:

$$e_{\partial C_y/\partial \alpha} = 2\sigma_{\partial \widetilde{C}_y/\partial \alpha}, \quad (5)$$

where  $\sigma$  is the standard deviation. The result of a typical Monte Carlo simulation to determine the uncertainty in  $\partial C_y / \partial \alpha$  is shown in Fig. 9. The shaded region indicates the range of  $\partial \widetilde{C}_y / \partial \alpha$  due to both the uncertainty in  $C_y$  and the numerical differentiation technique, and the error bars on the plot markers are obtained from Eq. (5).

## References

- Barrero-Gil, A., Sanz-Andrés, A., Alonso, G., 2009. Hysteresis in transverse galloping: the role of the inflection points. *J. Fluids Struct.* 25 (6), 1007–1020.
- Bergeron, K., Ecklebe, D., McClure, K., Johari, H., Curlett, T., Pitman, B., 2009. Parachute suspension line drag analysis. In: 20th AIAA Aerodynamic Decelerator Systems Technology Conference and Seminar, Vol. 2982.
- Blevins, R.D., 2001. *Flow-Induced Vibration*, second ed. Krieger Publishing Company.
- Carassale, L., Freda, A., Marrè-Brunenghi, M., 2014. Experimental investigation on the aerodynamic behavior of square cylinders with rounded corners. *J. Fluids Struct.* 44, 195–204.
- Feero, M.A., Naguib, A.M., Koochesfahani, M.M., 2019. Single-component force balance for the measurement of low-magnitude mean aerodynamic loads. *Meas. Sci. Technol.* 30 (11), 115301.
- Feero, M.A., Naguib, A.M., Koochesfahani, M.M., 2020. Influence of geometry on the galloping instability of rectangular cylinders in the reynolds number range 1,000–10,000. *J. Fluids Struct.* 94, 102881.
- Hansen, K.L., Kelso, R.M., Dally, B.B., 2011. Performance variations of leading-edge tubercles for distinct airfoil profiles. *AIAA J.* 49 (1), 185–194.
- Kalan, K., Feero, M., Naguib, A.M., Koochesfahani, M., 2020. Influence of surface topology on boundary layer and near-wake behavior of rectangular cylinders. In: *AIAA Scitech 2020 Forum*, Vol. 2020–2034.
- Kalan, K., Safaripour, A., Naguib, A.M., Koochesfahani, M.M., 2021. Characterization of the aerodynamics of rectangular cylinders with surface topology, Manuscript accepted for presentation at AIAA SciTech 2021 conference.
- Nakamura, Y., Tomonari, Y., 1977. Galloping of rectangular prisms in a smooth and in a turbulent flow. *J. Sound Vib.* 52 (2), 233–241.
- Naudascher, E., Rockwell, D., 2009. *Flow-Induced Vibrations*. CRC Press.
- Novak, M., 1972. Galloping oscillations of prismatic structures. *J. Eng. Mech. Div.* 98 (1), 27–46.
- Parkinson, G., 1989. Phenomena and modelling of flow-induced vibrations of bluff bodies. *Prog. Aerosp. Sci.* 26 (2), 169–224.
- Parkinson, G., Wawzonek, M., 1981. Some considerations of combined effects of galloping and vortex resonance. *J. Wind Eng. Ind. Aerodyn.* 8 (1–2), 135–143.
- Siefers, T., Greene, K., McLaughlin, T., Bergeron, K., 2013. Wind and water tunnel measurements of parachute suspension line. In: 51st AIAA Aerospace Sciences Meeting, Vol. AIAA 2013-0064.
- Siefers, T.M., McLaughlin, T.E., Bergeron, K., 2014. Wind tunnel characterization of fluid-structure interactions for various suspension lines. In: 44th AIAA Fluid Dynamics Conference, Vol. AIAA 2014-2771.
- Stoyanoff, S., 2001. A unified approach for 3d stability and time domain response analysis with application of quasi-steady theory. *J. Wind Eng. Ind. Aerodyn.* 89 (14–15), 1591–1606.